Highly Efficient Generation of Angular Momentum with Cylindrical Bianisotropic Metasurfaces

Junfei Li, Ana Díaz-Rubio, Chen Shen, Zhetao Jia, Sergei Tretyakov, and Steven Cummer

Phys. Rev. Applied **11**, 024016 — Published 6 February 2019

DOI: 10.1103/PhysRevApplied.11.024016

Highly Efficient Generation of Angular Momentum with Cylindrical Bianisotropic Metasurfaces

Junfei Li[1], Ana Díaz-Rubio[2], Chen Shen[1], Zhetao Jia[1], Sergei Tretyakov[2], and Steven Cummer[1]
[1]*Department of Electrical and Computer Engineering, Duke University, Durham, North Carolina 27708, USA*
[2]*Department of Electronics and Nanoengineering, Aalto University, P. O. Box 15500, FI-00076 Aalto, Finland*
(Dated: January 15, 2019)

Recent advances in metasurfaces have shown the importance of controlling the bianisotropic response of the constituent meta-atoms for maximum efficiency wavefront transformation. By carefully designing the bianisotropic response of the metasurface, full control of the local transmission and reflection properties is enabled, opening new design avenues for creating reciprocal metasurfaces. Despite recent advances in the highly efficient transformation of both electromagnetic and acoustic plane waves, the importance of bianisotropic metasurfaces for transforming cylindrical waves is still unexplored. Motivated by the possibility of arbitrarily controlling the angular momentum of cylindrical waves, we develop a design methodology of a bianisotropic cylindrical metasurface that enables transformation of cylindrical waves for both acoustic and electromagnetic waves with theoretically 100% power efficiency. This formalism is further validated in the acoustic scenario where the first experimental demonstration of highly efficient angular momentum transformation is shown.

I. INTRODUCTION

Metamaterials have been serving as a primary approach to fully control the behavior of electromagnetic waves, acoustic waves and elastic waves in recent years [1, 2], and is at present a highly active research area. Metasurfaces, as the 2D version of metamaterials, have opened up unprecedented possibilities for controlling waves at will, offering a solution of molding wave propagation within a planar geometry [3, 4]. By engineering the local phase shift in the unit cells, various functionalities have been achieved by metasurfaces, such as focusing [5], wave redirection and retro-reflection [6–8], enhanced absorption [9], cloaking [10], and holographic rendering [11, 12], to name a few. However, the efficiency of phase-gradient metasurfaces is fundamentally limited by the impedance mismatch between incident field and reflected/transmitted field, so that some of the energy is scattered into unwanted higher order diffracted modes, which hinders their applicability in various scenarios.

Recent advances have demonstrated that for electromagnetic and acoustic waves, full control of refraction or reflection can be achieved by carefully controlling the bianisotropy [13–19], also called Willis coupling in elastodynamics [20], in the unit cells. By tuning both transmitted and reflected phase profiles, one can not only control the microscopic phase profile along the metasurface but also achieve the overall macroscopic impedance match between the incident and scattered fields. Such metasurfaces, i.e., bianisotropic gradient metasurfaces, serve as the second generation of metasurfaces for wavefront manipulation [21]. In recent studies of wave deflection with both electromagnetic and acoustic bianisotropic gradient metasurfaces, it has been shown that the transmission efficiency can be significantly improved, especially for large deflection angles. Also, it has been demonstrated that bianisotropic gradient metasurfaces offer scattering-free wave manipulation even with a relatively coarse piecewise approximation of the required impedance matrix profile [19], which provides advantages in fabrication. However, the concept of bianisotropic metasurfaces and systematic design for scattering-free manipulation have only been explored in flat interfaces. Cylindrical topologies are among the most commonly used structures in electromagnetics, acoustics, and elastodynamics. The concept and benefits of bianisotropic metasurfaces, however, have not been extended to this field yet.

In analogy to anomalous refraction for flat metasurfaces, one of the possibilities offered by cylindrical metasurfaces is the transformation between different cylindrical waves. This transformation was achieved by locally controlling the phase profile along the surface and contribute to the generation of source illusion [22]. Generation of angular-momentum waves using a single metasurface layer designed with the generalized Snell's law (GSL) will not only introduce a large impedance mismatch but will also require a fine discretization of the surface which is not easily achievable by conventional cell architectures. Therefore, generation of wave fields with a large angular momentum still remains challenging. The successful realization of scattering-free bianisotropic planar metasurfaces suggests that scattering-free cylindrical metasurfaces might be possible.

There are numerous application possibilities offered by angular momentum-controlling metasurfaces beyond the source illusion mentioned above. Recent research has also demonstrated the manipulation of beams for particle trapping [23, 24] and boosting communication efficiency [25, 26] with acoustic angular momentum. Passive generation of wave fields with non-zero angular momentum is typically implemented by aperture design, leaky wave antennas or metasurfaces based on GSL [22, 27–29] for acoustic waves and inhomogeneous anisotropic media [30], spatial light modulator or spiral phase plates [31, 32]

for electromagnetic waves. However, the recent advances in metasurfaces for wavefront manipulation have shown that if only the transmission phase profile is controlled, parasitic scattering will inevitably appear, which reduces the efficiency, or even cause the structures fail to realize the desired functionalities, especially for large angular momentum.

In this paper, we present the first theoretical study, simulation, and experimental demonstration of highly efficient angular momentum generation by cylindrical bianisotropic metasurfaces. In particular, the work is focused on metasurfaces for the manipulation of cylindrical acoustic waves (see APPENDIX A for the electromagnetic counterpart). First, we theoretically analyze the generation of angular momentum showing that bianisotropic response is required for wavefront transformation with 100% power efficiency. Next, we propose a possible realization of the required impedance matrix profile. We take an example of the transformation between a point source (zero angular momentum) and a field with an angular momentum $n = 12$ and confirm in simulations that the desired field distribution is indeed created without any reflection and scattering. Finally, a realization in acoustics is verified by experiments.

II. THEORETICAL FORMULATION

For acoustic waves in homogeneous media, the 2D wave equation in the cylindrical coordinates is written as

$$\nabla^2 p = \frac{1}{r}\frac{\partial}{\partial r}\left(\frac{\partial p}{\partial r}\right) + \frac{1}{r^2}\frac{\partial^2 p}{\partial \varphi^2} = \frac{1}{c_0^2}\frac{\partial^2 p}{\partial t^2}, \tag{1}$$

where p is the acoustic pressure and c_0 is the sound speed in the background medium. Just like plane waves in Cartesian coordinates, Bessel-like spinning waves with different angular momentum serve as the bases in cylindrical coordinates. In the general case, the solution to this equation can be written as

$$p = \sum_n \left[a_n H_n^{(1)}(kr) + b_n H_n^{(2)}(kr)\right] e^{\mathrm{j}n\varphi} e^{\mathrm{j}\omega t}, \tag{2}$$

where $H_n^{(1)}$ denotes the Hankel function of the first kind (waves converging to the center) and $H_n^{(2)}$ denotes the Hankel function of the second kind (waves diverging from the center), index n represents the angular momentum, a_n and b_n are the amplitudes of the waves, and $k = \omega/c_0$ is the wavenumber at the frequency of interest. The assumed time dependence for the monochromatic wave is $e^{j\omega t}$, and it will be omitted throughout the paper for brevity.

In this section we will discuss the theoretical requirements for a metasurface to produce perfect transformation between cylindrical waves with different angular momenta, i.e. with different spinning characteristics, as it is shown in Fig. 1. The term perfect is in the sense of wavefront transformation with 100% power efficiency. The

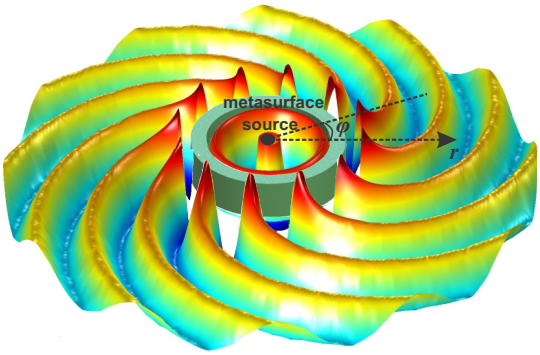

FIG. 1. Illustration of the desired performance of a metasurface to convert the inner field to a prescribed outer field without parasitic scattering

derivation of the solution will be presented considering acoustic waves, however, a similar formulation can be used for electromagnetic waves (see APPENDIX A).

The formulation of the problem starts with the definition of the fields inside and outside the volume bounded by the metasurface. Let us consider the field in Medium I (inside the metasurface) and Medium II (outside the volume bounded by the metasurface) as divergent waves with the angular momentum n_1 and n_2 that can be expressed as

$$p^{\mathrm{I,II}} = p_{1,2} H_{n_{1,2}}^{(2)}(kr) e^{\mathrm{j}n_{1,2}\varphi}, \tag{3}$$

where $p_{1,2}$ are the amplitudes for the incident and transmitted waves. In general, both amplitudes are complex. However, for arbitrarily given complex wave amplitudes, we can always rotate the coordinate system and pick a start time such that both complex amplitudes become real. Such an operation will simplify the derivation but wont affect the generality, and it wont affect the final designed structure as well. It is important to mention that we only consider a divergent wave inside the metasurface because the objective of the metasurface is to completely transform the incident cylindrical wave without reflections. The velocity vector can be calculated from the pressure field ($\vec{v} = \frac{\mathrm{j}}{\omega\rho}\nabla p$) as

$$\vec{v}^{\mathrm{I,II}} = \frac{p_{1,2}}{Z_0}\left[\mathrm{j}\partial_r H_{n_{1,2}}^{(2)}(kr)\hat{\rho} - \frac{n_{1,2}}{kr} H_{n_{1,2}}^{(2)}(kr)\hat{\varphi}\right] e^{\mathrm{j}n_{1,2}\varphi}, \tag{4}$$

where $Z_0 = \rho c_0$ is the characteristic impedance of air and ∂_r represents the partial derivative with respect to r.

We assume that the metasurface is a cylindrical tube whose axis is located at the origin, with inner radius and outer radius being r_1 and r_2, respectively. For lossless and scattering-free metasurfaces, the energy conservation condition shall be met. Denoting the time-averaged intensity vector as

$$\vec{I} = \frac{1}{2}\mathrm{Re}\left\{p\vec{v}^*\right\} = I_r\hat{\rho} + I_\varphi\hat{\varphi}, \tag{5}$$

this condition can be expressed in terms of the radial components of this vector at the two sides of the metasurface:

$$I_r^{\mathrm{I}} = \frac{p_1^2}{2Z_0}\left[J_{n_1}(kr)\partial_r Y_{n_1}(kr) - Y_{n_1}(kr)\partial_r J_{n_1}(kr)\right]|_{r_1} \quad (6)$$

$$I_r^{\mathrm{II}} = \frac{p_2^2}{2Z_0}\left[J_{n_2}(kr)\partial_r Y_{n_2}(kr) - Y_{n_2}(kr)\partial_r J_{n_2}(kr)\right]|_{r_2} \quad (7)$$

where J_α and Y_α represent the Bessel functions of the first and second kind, respectively. These expressions can be simplified as

$$I_r^{\mathrm{I}} = \frac{p_1^2}{\pi Z_0}\frac{1}{r_1} \quad (8)$$

$$I_r^{\mathrm{II}} = \frac{p_2^2}{\pi Z_0}\frac{1}{r_2}. \quad (9)$$

To ensure that all the energy of the incident wave is carried away by the transmitted spinning wave, the normal component of the intensity vector crossing a line segment of the inner radius, $S_1 = r_1 \mathrm{d}\varphi$, has to be equal to the one crossing the corresponding line segment in the other radius, $S_2 = r_2 \mathrm{d}\varphi$. This condition can be written as $I_r^{\mathrm{I}} S_1 = I_r^{\mathrm{II}} S_2$, which yields $p_2 = p_1$. If we define the macroscopic transmission coefficient as

$$T = \frac{p^{\mathrm{II}}(r_2)}{p^{\mathrm{I}}(r1)} = \frac{H_{n_2}^{(2)}(kr_2)}{H_{n_1}^{(2)}(kr_1)} e^{j(n_2-n_1)\varphi}, \quad (10)$$

it is possible to see that if $|n_2| > |n_1|$, the magnitude of macroscopic transmission coefficient can be greater than one when $|H_{n_2}^{(2)}(kr_2)| > |H_{n_1}^{(2)}(kr_1)|$, given the fact that waves with larger angular momentum decay slower along the radial direction. The feature of transmission coefficient greater than one can never be realized by phase engineering only. It is noted here that this condition is analogous to the plane-wave case described in [18, 19].

The next step towards the realization of perfect transformation between cylindrical waves is to determine the required boundary conditions at both sides of metasurface. At the inner and outer boundaries of the metasurface, for each specific circumferential position, the impedance matrix which models the metasurface is defined as

$$\begin{bmatrix} p^{\mathrm{I}}(r_1,\phi) \\ p^{\mathrm{II}}(r_2,\phi) \end{bmatrix} = \begin{bmatrix} Z_{11} & Z_{12} \\ Z_{21} & Z_{22} \end{bmatrix} \begin{bmatrix} S_1 \hat{n}\cdot\vec{v}^{\mathrm{I}}(r_1,\phi) \\ -S_2 \hat{n}\cdot\vec{v}^{\mathrm{II}}(r_2,\phi) \end{bmatrix}, \quad (11)$$

where $\hat{n}$ is the unit normal vector to the metasurface. Such a system can be viewed as a two-port network, which can be represented by an equivalent circuit. In the most general linear, time-invariant, and reciprocal case, the impedance matrix is symmetric, $Z_{12} = Z_{21}$. If we further assume that the system is lossless where the equivalent circuit is composed of only capacitors and inductors without resistors or other dissipative elements, the resulting impedance matrix is purely imaginary, i.e., $Z_{ij} = jX_{ij}$.

For compactness, we denote

$$C_{n_1} = H_{n_1}^{(2)}(kr_1)e^{\mathrm{j}n_1\phi} \quad (12)$$

$$C_{n_2} = H_{n_2}^{(2)}(kr_2)e^{\mathrm{j}n_2\phi} \quad (13)$$

$$C'_{n_1} = \frac{1}{2}[H_{n_1-1}^{(2)}(kr_1) - H_{n_1+1}^{(2)}(kr_1)]e^{\mathrm{j}n_1\phi} \quad (14)$$

$$C'_{n_2} = \frac{1}{2}[H_{n_2-1}^{(2)}(kr_2) - H_{n_2+1}^{(2)}(kr_2)]e^{\mathrm{j}n_2\phi}. \quad (15)$$

Substituting the assumed pressure field and velocity field for the incident wave and transmitted wave into Eq. (11) and employing the recurrence relation for Hankel functions, namely $dH_\alpha^{(1,2)}(x)/dx = [H_{\alpha-1}^{(1,2)}(x) + H_{\alpha+1}^{(1,2)}(x)]/2$, Eq. (11) can be rewritten in form of a system of two linear equations:

$$\begin{cases} Z_0 C_{n_1} = -S_1 X_{11} C'_{n_1} + S_2 X_{12} C'_{n_2} \\ Z_0 C_{n_2} = -S_1 X_{12} C'_{n_1} + S_2 X_{22} C'_{n_2} \end{cases} \quad (16)$$

After some algebra, the components of the impedance matrix can thus be calculated:

$$X_{11} = \frac{Z_0}{S_1}\frac{\mathrm{Im}(C_{n_1})\mathrm{Re}(C'_{n_2}) - \mathrm{Re}(C_{n_1})\mathrm{Im}(C'_{n_2})}{\mathrm{Im}(C'_{n_2})\mathrm{Re}(C'_{n_1}) - \mathrm{Re}(C'_{n_2})\mathrm{Im}(C'_{n_1})} \quad (17)$$

$$X_{22} = \frac{Z_0}{S_2}\frac{\mathrm{Im}(C_{n_2})\mathrm{Re}(C'_{n_1}) - \mathrm{Re}(C_{n_2})\mathrm{Im}(C'_{n_1})}{\mathrm{Im}(C'_{n_2})\mathrm{Re}(C'_{n_1}) - \mathrm{Re}(C'_{n_2})\mathrm{Im}(C'_{n_1})} \quad (18)$$

$$X_{12} = -\frac{Z_0}{S_1}\frac{\mathrm{Im}(C'_{n_2})\mathrm{Re}(C_{n_2}) - \mathrm{Re}(C'_{n_2})\mathrm{Im}(C_{n_2})}{\mathrm{Im}(C'_{n_2})\mathrm{Re}(C'_{n_1}) - \mathrm{Re}(C'_{n_2})\mathrm{Im}(C'_{n_1})}. \quad (19)$$

For simplicity in the derivations, and to provide another view point for the requirements, the required properties of the metasurface can also be expressed in terms of the transfer matrix, which is defined by

$$\begin{bmatrix} p^{\mathrm{I}}(r_1,\phi) \\ S_1 \hat{n}\cdot\vec{v}^{\mathrm{I}}(r_1,\phi) \end{bmatrix} = \begin{bmatrix} M_{11} & M_{12} \\ M_{21} & M_{22} \end{bmatrix} \begin{bmatrix} p^{\mathrm{II}}(r_2,\phi) \\ S_2 \hat{n}\cdot\vec{v}^{\mathrm{II}}(r_2,\phi) \end{bmatrix} \quad (20)$$

Conversion from the impedance matrix to the transfer matrix is given by

$$M = \begin{bmatrix} \frac{Z_{11}}{Z_{21}} & \frac{Z_{11}Z_{22}-Z_{21}Z_{12}}{Z_{21}} \\ \frac{1}{Z_{21}} & \frac{Z_{22}}{Z_{21}} \end{bmatrix} \quad (21)$$

which indicates that M_{11} and M_{22} are real, while M_{12} and M_{21} are imaginary. Explicit solution for the transfer matrix are expressed as:

$$M_{11} = \frac{\mathrm{Im}(C'_{n_2})\mathrm{Re}(C_{n_1}) - \mathrm{Re}(C'_{n_2})\mathrm{Im}(C_{n_1})}{\mathrm{Im}(C'_{n_2})\mathrm{Re}(C_{n_2}) - \mathrm{Re}(C'_{n_2})\mathrm{Im}(C_{n_2})} \quad (22)$$

$$M_{22} = \frac{-S_1}{S_2}\frac{\mathrm{Im}(C_{n_2})\mathrm{Re}(C'_{n_1}) - \mathrm{Re}(C_{n_2})\mathrm{Im}(C'_{n_1})}{\mathrm{Im}(C'_{n_2})\mathrm{Re}(C_{n_2}) - \mathrm{Re}(C'_{n_2})\mathrm{Im}(C_{n_2})} \quad (23)$$

$$M_{12} = \frac{\mathrm{j}Z_0}{S_2}\frac{\mathrm{Im}(C_{n_2})\mathrm{Re}(C_{n_1}) - \mathrm{Re}(C_{n_2})\mathrm{Im}(C_{n_1})}{\mathrm{Im}(C'_{n_2})\mathrm{Re}(C_{n_2}) - \mathrm{Re}(C'_{n_2})\mathrm{Im}(C_{n_2})} \quad (24)$$

$$M_{21} = \frac{\mathrm{j}S_1}{Z_0}\frac{\mathrm{Im}(C'_{n_2})\mathrm{Re}(C'_{n_1}) - \mathrm{Re}(C'_{n_2})\mathrm{Im}(C'_{n_1})}{\mathrm{Im}(C'_{n_2})\mathrm{Re}(C_{n_2}) - \mathrm{Re}(C'_{n_2})\mathrm{Im}(C_{n_2})}. \quad (25)$$

It can be easily checked that this matrix corresponds to a reciprocal and lossless system.

Note that as long as $|n_1| \neq |n_2|$, we will always have $M_{11} \neq M_{22}$, which leads to $Z_{11} \neq Z_{22}$ for a infinitely

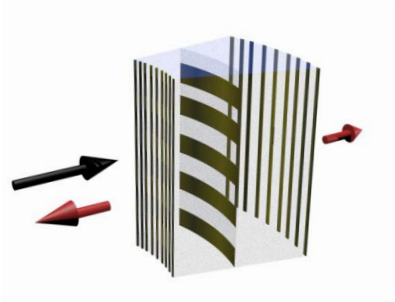

FIG. 2. Schematic representation of a multilayer system with fully controllable asymmetric response.

thin surface ($r_1 = r_2$), which indicates carefully designed asymmetric response shall be provided by the unit cell. Discussion about metasurface with a finite thickness can be found in APPENDIX B. This asymmetry is analogous to the plane-wave case in the Cartesian coordinates, meaning that controlling only the transmission phase along the metasurface is not enough for full control of the power flow. Instead, a bianisotropic metasurface with precisely controlled asymmetric response is required.

III. DESIGN AND REALIZATION OF CYLINDRICAL BIANISOTROPIC METASURFACES

For the actual implementation of the metasurface described in the previous section, there are several different possible approaches.

A. Multilayer model

The analysis of a cylindrical metasurfaces with infinitesimal thickness capable of perfectly transforming the scattered wavefronts shows that bianisotropic response is needed. Such response can be obtained by controlling the electromagnetic coupling for EM waves or the Willis coupling in the acoustic counterpart. Looking into the scattering characteristics of such particles, one can see that the bianisotropic response is translated into asymmetric reflection from the backward and forward directions with same magnitude but different phases. Due to the small size required for the implementation of bianisotropic gradient metasurfaces, an extended way to fully control the asymmetric response of the particles is to cascade multiple impedance layers.

1. Electromagnetic metasurfaces

For the electromagnetic case, one can consider a cascade of metallic pattern separated by concentric dielectric substrates [see Figure 2]. The patterned metallic sheets can be modeled as shunt impedances with the following transfer matrix

$$M_{Zi} = \begin{bmatrix} 1 & 0 \\ Y_i & 1 \end{bmatrix}, i = 1, 2, 3 \tag{26}$$

where $Y_i = 1/Z_i$ represents the effective impedance of the metallic patterns. On the other hand the transmission matrix of the of a wedge-shaped dielectric sector can be expressed as

$$M_{Ti} = \begin{bmatrix} A_i & B_i \\ C_i & D_i \end{bmatrix}, i = 1, 2 \tag{27}$$

The values of the matrix elements are functions of the inner and outer radii and the dielectric permittivity ε_d (see APPENDIX B for more information). Finally the total transmission matrix can be calculated as

$$M = \begin{bmatrix} M_{11} & M_{12} \\ M_{21} & M_{22} \end{bmatrix} = M_{Z1} M_{T1} M_{Z2} M_{T2} M_{Z3} \tag{28}$$

After some algebra, we can obtain the required sheet admittances (Y_1, Y_2, and Y_3) as a function of the required scattering properties (M_{11}, M_{12}, M_{21}, and M_{22})

$$Y_2 = \frac{M_{12} - B_1 D_2 - A_1 B_2}{B_1 B_2} \tag{29}$$

$$Y_1 = \frac{M_{22} - (D_1 D_2 + C_1 B_2 + D_1 B_2 Y_2)}{A_1 B_2 + B_1 D_2 + B_1 B_2 Z_2} \tag{30}$$

$$Y_3 = \frac{M_{11} - (B_1 C_2 + A_1 A_2 + B_1 A_2 Y_2)}{A_1 B_2 + B_1 D_2 + B_1 B_2 Y_2} \tag{31}$$

At microwave frequency the required sheet admittances can be implemented by using metallic patterns [33].

2. Acoustic models

For the acoustic scenario, the asymmetric response can be obtained as cascade of three different membranes separated by a certain distance. The response of a meta-atom can be expressed in terms of the transmission matrices

$$M = M_{Z1} M_{T1} M_{Z2} M_{T2} M_{Z3} \tag{32}$$

with

$$M_{Zi} = \begin{bmatrix} 1 & Z_i \\ 0 & 1 \end{bmatrix}, i = 1, 2, 3 \tag{33}$$

and $M_{Ti}, i = 1, 2$ is the transfer matrix of a wedge-shaped sector, which is a function of its inner and outer radius. Detailed derivation of the explicit expression of M_{Ti} can be found in APPENDIX B. Here for simplicity, let us denote

$$M_{Ti} = \begin{bmatrix} A_i & B_i \\ C_i & D_i \end{bmatrix}, i = 1, 2 \tag{34}$$

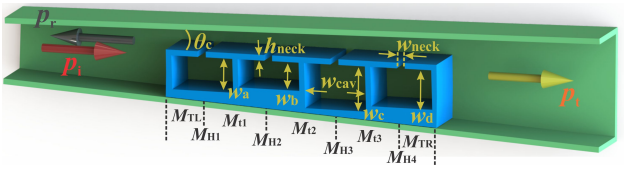

FIG. 3. Unit cell consisting four resonators for the realization of the impedance matrix in cylindrical coordinates.

Then the required impedances for the three membranes can be calculated as

$$Z_2 = \frac{M_{21} - C_1A_2 - D_1C_2}{C_1C_2} \tag{35}$$

$$Z_1 = \frac{M_{11} - (A_1A_2 + B_1C_2 + A_1C_2Z_2)}{C_1A_2 + D_1C_2 + C_1C_2Z_2} \tag{36}$$

$$Z_3 = \frac{M_{22} - (C_1B_2 + D_1D_2 + C_1D_2Z_2)}{C_1A_2 + D_1C_2 + C_1C_2Z_2} \tag{37}$$

B. Channel with side-loaded resonators

By controlling the thickness and in-plane tension of the membranes, one can, in principle, control the impedances to satisfy Eqs. (17)-(19). However, the surface tension, uniformity and durability for the membranes are extremely hard to control, and it is questionable whether such configuration can be practically realized.

An alternative approach based on a straight channel with four resonators was proposed for flat surfaces [19]. The design provides enough degrees of freedom for full control over the bianisotropic response while reducing the loss induced by resonances. Here, we propose the four-resonator design in cylindrical coordinates for full control over the bianisotropic response of the unit cells. An examplary cell is shown in Fig. 3. In this structure the width and the height of the neck $w_{\rm neck} = 1.5$ mm and $h_{\rm neck} = 1$ mm are fixed for the four resonators. The wall thickness between the resonators is 1 mm, and the width of the cavities $w_{cav} = 11.5$ mm is also fixed; the sector angle of the wedge-shaped channel θ_c and the height of the resonators $w_{\rm a}$, $w_{\rm b}$, $w_{\rm c}$, and $w_{\rm d}$ can be varied to control the overall impedance response; and the wall thickness of the unit cell is fixed and will be defined by the fabrication limitations. The walls between adjacent cells are assumed to be hard so that the wave does not propagate along the orthogonal direction inside the metasurface. Therefore, all the cells in the bianisotropic metasurfaces can be designed individually.

The transfer matrix of the proposed meta-atom topology can be calculated as

$$M = M_{TL}M_{H1}M_{T1}M_{H2}M_{T2}M_{H3}M_{T3}M_{H4}M_{TR} \tag{38}$$

with M_{TL}, M_{TR}, and $M_{T1,2,3}$ being the transfer functions of transmission lines at the entrance, exit, and between adjacent resonators, as is shown in Fig. 3. M_{Hi} are the transfer matrices of each individual resonator and are expressed as

$$M_{Hi} = \begin{bmatrix} 1 & 0 \\ 1/Z_{Hi} & 1 \end{bmatrix}, \qquad i = 1, 2, 3, \tag{39}$$

where Z_{Hi} are the acoustic impedances for each shunted resonator. The detailed derivation of $Z_{\rm Hi}$ is given in [34].

The impedance matrix of an arbitrary meta-atom can then be calculated by converting the transfer matrix using

$$Z = \begin{bmatrix} \frac{M_{11}}{M_{21}} & \frac{M_{11}M_{22} - M_{21}M_{12}}{M_{21}} \\ \frac{1}{M_{21}} & \frac{M_{22}}{M_{21}} \end{bmatrix}. \tag{40}$$

With the theoretical requirement for perfect wavefront transformation and the versatility of the meta-atom for full control over the bianisotropic response, the next step is to decide the detailed physical dimensions of the meta-atoms that form the metasurface. Since there are three independent elements in the required impedance matrix (X_{11}, X_{12}, X_{22}) and five controlling parameters (θ_c, $w_{\rm a}$, $w_{\rm b}$, $w_{\rm c}$ and $w_{\rm d}$), there can be many combinations for a meta-atom to realize the required impedance matrix. To solve for a practical design within geometrical limitations, a continuous genetic algorithm (GA) is adopted for optimization of the design parameters, so that the impedance matrix of the optimized structure matches the theoretical requirements. In the algorithm, we minimize the cost function, which is the relative error between the impedance matrix for the unit cell and the theoretically required impedance matrix at each point, defined as

$$\text{cost} = \sqrt{\sum_{i,j} \left| \frac{Z_{ij}^{\rm str} - Z_{ij}^{\rm req}}{Z_{ij}^{\rm req}} \right|^2} \tag{41}$$

where "str" stands for impedance matrix of the structure and "req" stands for the theoretical requirements. $i, j = 1, 2$ denote each element in the matrix.

We have designed a metasurface to transform a monopole source ($n_1 = 0$) located at the center to a spinning field with the angular momentum of $n_2 = 12$. In this case, $r_1 = 15$ cm, $r_2 = 20$ cm, and one period is represented by 6 meta-atoms. In this case, each unit cell occupies a sector of $\Delta\phi = \pi/36$, therefore, $S_1 = \Delta\phi r_1$ and $S_2 = \Delta\phi r_2$. We swept the circumferential positions with a step of 0.1 degrees, and run the GA optimization 50 times at each point to search for the best combination with the lowest relative error.

Although theoretical calculation offers a fast and close approximation of the meta-atom behavior, it will also introduce some error due to truncation of the infinite series and the straight channel assumption. On the other hand, extracting the impedance using commercial simulations (for example, COMSOL Multiphysics) offers slow but more precise characterization. Therefore, based on the structure obtained from theoretical optimization,

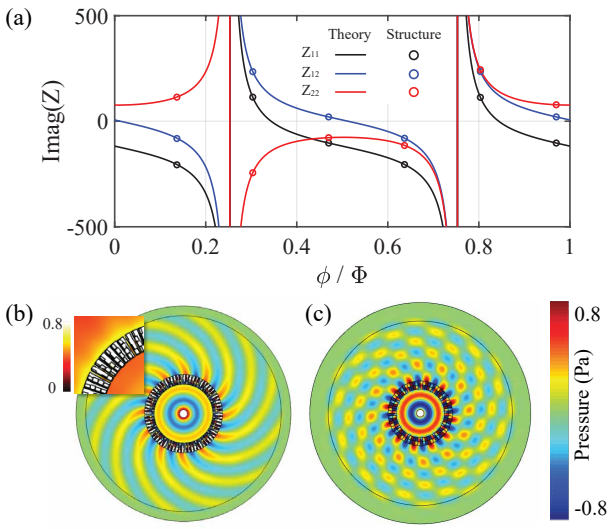

FIG. 4. Theoretically determined and optimized impedances and the simulated fields. (a) Comparison between theoretical requirements and the achieved values using GA optimization. (b) The real part of the simulated acoustic field using real structures. The inset shows the pressure amplitude near the metasurface. (c) The field generated by GSL based metasurface using ideal unit cells as a comparison.

we further optimize it locally using genetic algorithm by slightly perturbing the structure dimensions within ± 1 mm. The method used for extracting the impedance matrix from simulation was adopted from the standard "4-microphone" method.

The method uses four microphones to measure the pressure at two fixed points on both sides of the tested structure under two different boundary conditions, and the properties can be calculated accordingly. Based on the same idea, we developed a method to extract the structure properties in cylindrical coordinates. Detailed derivation of the method is summarized in APPENDIX D.

The theoretical requirement for the desired metasurface and the achieved values from the two-step optimization is shown in Fig. 4(a). Detailed dimensions of the meta-atoms and their relative errors can be found in Table I. We can see that the required impedance is accurately realized by the optimized meta-atoms. Simulation of the obtained structure was performed in COMSOL Multiphysics with the pressure acoustics module. The walls of the unit cells are set to be hard due to the large impedance contrast in the implementation. The background medium is air with density 1.21 kg/m^3 and sound speed 343 m/s. The incident pressure amplitude is 1 Pa at $r = 2$ cm. The outer edge of the simulated region is connected to a perfectly matched layer. The simulated pressure field and the pressure amplitude are shown in Fig. 4(b). We can see that the monopole wavefront is nearly perfectly converted to a field with the angular momentum of 12 without parasitic reflection and scattering. Remarkably, from the pressure amplitude field we can see that the macroscopic transmission coefficient $|T| > 1$. This means that the pressure on the transmission side is larger than the incident side, which is in agreement with the theoretical analysis. The corresponding reference GSL metasurface formed by ideal unit cells with the same size and the same number of cells period is shown in Fig. 4(c) as a comparison. Here the ideal GSL unit cells are defined as the unit cells whose transmission coefficient has the amplitude 1 and precisely controlled phase, i.e., the scattering matrix for an ideal unit cell is expressed as:

$$S = \begin{bmatrix} 0 & e^{j\Phi_t} \\ e^{j\Phi_t} & 0 \end{bmatrix} \tag{42}$$

where $\Phi_t = n\phi$ denotes the desired transmission phase along the metasurface. By converting the scattering matrix into transfer matrix (APPENDIX. C), the multilayer model in Sec. III A can be applied to realize such an ideal scattering property in simulation. From Fig. 4(c) we can see that there is strong reflection and lots of the transmitted energy is scattered to the unwanted modes and the overall wave pattern is corrupted.

TABLE I. **Design parameters of the meta-atoms**

Cell	cost(%)	θ_c (mm)	w_a (mm)	w_b (mm)	w_c (mm)	w_d (mm)
1	2.08	0.5699	6.8	8.8	8.6	6.9
2	0.66	0.5655	7.0	7.0	8.3	6.4
3	0.16	0.6997	8.4	7.9	2.5	5.2
4	0.55	0.7002	7.4	8.4	0.9	4.3
5	0.35	1.0221	4.1	8.1	6.7	3.0
6	0.84	1.3931	8.7	2.1	0.5	3.0

IV. EXPERIMENTAL VERIFICATION.

The theory and simulations are then verified with experiments. We choose the same scenario discussed in the previous section. The experimental setup is shown in Fig. 5(a). The sample was fabricated by Selective Laser Sintering (SLS) 3D-printing. The material is nylon with a density of 950 kg/m^3 and sound speed of 1338 m/s, so that the walls can be regarded as acoustically rigid due to the large impedance contrast with air. The printed sample has the inner radius of 150 mm and the outer radius of 200 mm, and the height of the sample is 41 mm to fit in the 2D waveguide. The overall size of the 2D waveguide is 1.2 m by 1.2 m. The monopole source was provided by a 1-inch speaker located at the center, which sends a Gaussian modulated pulse centered at 3000 Hz. At each scanned point, the transmitted pulse was recorded by averaging the measurement 10 times to eliminate noise. The pulse is then time-gated to eliminate reflections from the boundaries. Then the complex field at each point is calculated by performing Fourier transform of the time-gated signal. The whole field was scanned by moving

the microphone with a step of 1 cm. Since the overall size of the scanning system is limited, a quarter of the whole field is scanned, as shown in Fig. 5(a), and the measured data is then mapped to other regions due to field symmetry.

The real part of the scanned field and the phase of the field is plotted in Fig 5(b) and Fig. 5(c), respectively. From the experimental results, we can see that the fabricated metasurface creates a field with much lower unwanted scattering compared with an ideal GSL-based metasurface shown in Fig. 5(d). The small discrepancies between simulation and experiment are due to fabrication tolerance and the small difference between the assumed and actual properties of air. In particular, the sound speed was 344 m/s in our lab during the measurement window, while we assumed 343 m/s in the simulation, which will cause the working frequency to increase by about 8 Hz. The small misalignment in the vertical and horizontal directions is caused by a small misalignment of the sample and the scanning stage. To quantitatively characterize the results, we extracted the coefficients of contributing modes by taking the measurements on a $r = 22$ cm circle centered at the source and performing a Fourier transform of the fields to extract the amplitudes of different modes. The power of each mode is calculated and then normalized by the total power. The power distribution over the modes of $n = -30$ to $n = 30$ is plotted in Fig. 5(d). For comparison, the same analysis is performed for the simulation of the bianisotropic metasurface and the ideal GSL-based metasurface. We can clearly see that the GSL-based metasurface, even with the perfectly designed cells of full transmission and precise control of the transmitted phase, produces a large component of $n = -12$ mode, and only 70% of the transmitted energy is in the desired mode. On the other hand, for the bianisotropic designs, the unwanted scattering is greatly suppressed, showing 99% and 92% of the transmitted energy in the desired mode $n = 12$ in simulation and experiment, respectively. The experimental results show good agreement with the simulation, demonstrating the possibility of near perfect transformation of acoustic wavefronts.

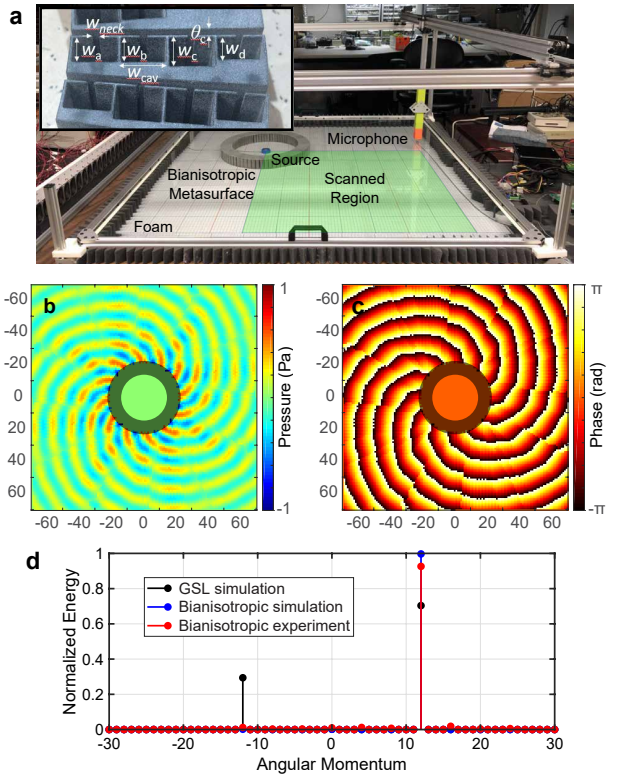

FIG. 5. Experimental setup and results. (a) A photo of the experimental setup. The field is scanned by moving the microphone in the green region. (b) The real part of the measured pressure field. (c) The phase of the scanned field. We can clearly see that the wavefront is nearly perfectly transformed to the field with the angular momentum $n = 12$. (d) The comparison among the bianisotropic metasurface in simulation and experiment, and the ideal GSL-based metasurface in the simulation. In the experiment, 92% of the transmitted energy is concentrated in the desired mode.

V. DISCUSSION

In this paper, we have introduced a multi-physics design method for creation of acoustic or electromagnetic bianisotropic metasurfaces of cylindrical shape for perfect generation of waves with arbitrary angular momenta. We first defined theoretically the conditions and requirements, and pointed out that controlling the local phase shift in transmission alone cannot achieve such transformations. Instead, full control over the reflection and transmission coefficient in both directions through bianisotropy is required. Then we proposed possible realizations for acoustic waves, and verified them with simulations, showing that the proposed metasurface nearly perfectly transforms a monopole source into a spinning wave field with the angular momentum of 12, which is beyond the ability of conventional GSL-based metasurfaces. Then we proposed a systematic and practical way of creating cylindrical bianisotropic acoustic metasurfaces and verified it with experiments. The experimental results show excellent agreement with simulations, with 92% of the transmitted energy concentrated in the desired mode, whereas with the use of an ideal GSL-based metasurface, 30% of the transmitted energy is scattered to other modes. Here we would like to note that the efficiency of the conventional GSL-based design is even lower because the simulation shows that 10% of the energy is reflected indicating that the ideal efficiency can reach only 63%, while our design is free of reflections.

The use of waves with non-zero angular momenta has shown great potential in high-speed communications, source illusion and particle manipulation in the fields of optics, electromagnetics, and acoustics. However, one obstacle is the efficiency of generating angular momentum, especially when the target angular momentum is

large. In this paper, we have proposed and demonstrated the realization of theoretically perfect generation of angular momenta with a bianisotropic metasurface. We also hope that such metasurfaces can be explored in optics to enhance the efficiency of generating orbital angular momentum beams for high-speed optical communications and other applications.

Here we would like to stress that the proposed design strategy is not only valid for generation of angular momentum beams but for the arbitrary manipulation of wavefronts, both for acoustic and electromagnetic waves. For example, by designing the bianisotropic impedance matrix profile, one may create a multi-polar sources from a single excitation within a limited space; the proposed metasurface may also be applied as an interface between two media to enhance energy transfer; the metasurface may also be applied in topological insulators to either act as a spinning source to excite some certain modes, or even provide the "pseudo spin" for topological insulators in airborne systems. We believe that the proposed bianisotropic metasurface concepts can serve as a new approach to designing highly efficient metasurfaces.

ACKNOWLEDGMENTS

This work was supported by the Multidisciplinary University Research Initiative grant from the Office of Naval Research (N00014-13-1-0631), an Emerging Frontiers in Research and Innovation grant from the National Science Foundation (Grant No. 1641084), and in part by the Academy of Finland (project 287894 and 309421).

APPENDIX A: ELECTROMAGNETIC FORMULATION OF THE CYLINDRICAL BIANISOTROPIC METASURFACE

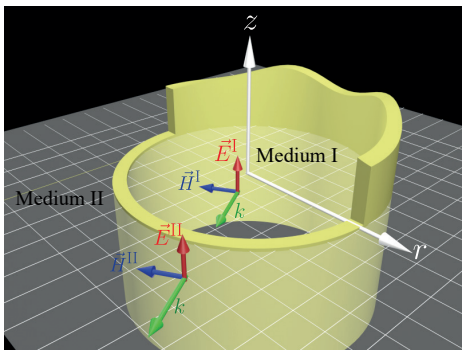

FIG. A1. Schematic representation electromagnetic system for TE-polarization.

Using a similar analysis to that the proposed in the main text, metasurfaces for perfect cylindrical transformations of electromagnetic wavefronts can be designed. For example, let us consider the TE-polarization case where electric field along z-direction, $\mathbf{E} = E_z\hat{z}$. The wave equation for TE-polarization can be written as

$$\frac{1}{r}\frac{\partial}{\partial r}\left(\frac{\partial E_z}{\partial r}\right) + \frac{1}{r^2}\frac{\partial^2 E_z}{\partial \varphi^2} = \frac{1}{c_0^2}\frac{\partial^2 E_z}{\partial t^2}. \quad \text{(A1)}$$

It is clear that this wave equation has the same form as the acoustic counterpart and consequently the solution can also be expressed as a combination of cylindrical waves emerging $[H_n^{(1)}(kr)]$ and diverging $[H_n^{(2)}(kr)]$ from the origin of coordinates with a certain angular momentum n.

We start by defining a diverging wave with angular momentum, n_1, in the Medium I that can be written as

$$E_z^{\mathrm{I}} = E_0 H_{n1}^{(2)}(kr)e^{jn_1\varphi}, \quad \text{(A2)}$$

where E_0 is the amplitude of the wave. It is easy to obtain the expression of the corresponding magnetic field by applying Maxwell equation ($\nabla \times \mathbf{E} = -j\omega\mu_0\mathbf{H}$). Finally, the magnetic field reads

$$\mathbf{H}^{\mathrm{I}} = -\frac{E_0}{Z_0}\left[\frac{n_1}{kr}H_{n1}^{(2)}(kr)\hat{r} + j\partial_r H_{n1}^{(2)}(kr)\hat{\varphi}\right]e^{jn_1\varphi}, \quad \text{(A3)}$$

with $Z_0 = \sqrt{\mu_0/\varepsilon_0}$ being the wave impedance in the background field. Following the same procedure, the field in Medium II will be defined as

$$E_z^{\mathrm{II}} = E_{\mathrm{t}} H_{n2}^{(2)}(kr)e^{jn_2\varphi}, \quad \text{(A4)}$$

where T is the transmission coefficient and n_2 is the angular momentum of the fields outside the metasurface. The expressions for the magnetic field in the Medium II is

$$\mathbf{H}^{\mathrm{II}} = \frac{E_{\mathrm{t}}}{Z_0}\left[\frac{n_2}{kr}H_{n2}^{(2)}(kr)\hat{r} + j\partial_r H_{n2}^{(2)}(kr)\hat{\varphi}\right]e^{jn_2\varphi}. \quad \text{(A5)}$$

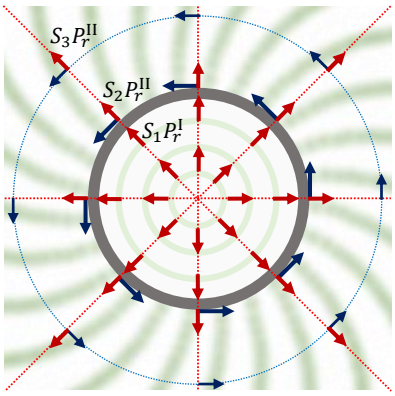

FIG. A2. Schematic representation of the Poynting vector distribution inside and outside the metasurface. Green patterns represent the wavefronts.

In order to realize cylindrical transformations with 100% power efficiency, it is necessary to ensure the fulfillment of the power conservation between the waves

inside and outside the metasurface. The Poynting vector of the cylindrical waves can be calculated as $\vec{P} = \frac{1}{2}\mathrm{Re}\left\{\vec{E}\times\vec{H}^*\right\} = P_r\hat{r} + P_\varphi\hat{\varphi}$, where

$$P_r = \frac{E_0^2}{\pi Z_0}\frac{1}{r} \tag{A6}$$

and

$$P_\varphi = \frac{E_0^2}{\pi Z_0}\frac{n}{kr}J_n(kr). \tag{A7}$$

The angular component of the Poynting vector, P_φ, represents the circumferential contour around the origin of coordinates (see Figure A2). Due to the inherent periodicity of the system in the angular direction, this component do not contribute to the global power balance. If we consider that the internal and external boundaries of the metasurface are located at r_1 and r_2, the condition for ensuring the power balance reads $S_1 P_r^{\mathrm{I}}|_{r_1} = S_2 P_r^{\mathrm{II}}|_{r_2}$. Finally, the amplitude of transmitted waves should satisfy $E_{\mathrm{t}} = E_0$.

Once the desired waves are fully defined, one has to relate the fields at both sides of the metasurface as follows

$$\begin{bmatrix} E^{\mathrm{I}}(r_1,\varphi) \\ E^{\mathrm{II}}(r_2,\varphi)\end{bmatrix} = \begin{bmatrix} Z_{11} & Z_{12} \\ Z_{12} & Z_{22}\end{bmatrix}\begin{bmatrix} S_1\hat{n}\times H^{\mathrm{I}}(r_1,\varphi) \\ -S_2\hat{n}\times H^{\mathrm{II}}(r_1,\varphi)\end{bmatrix} \tag{A8}$$

where $\hat{n}$ is the normal vector to the metasurface and the matrix $[Z]$ defines the electromagnetic properties of the metasurface. It is important to notice that the off-diagonal terms of the impedance matrix are forced to be equal, meaning that we will inspect only reciprocal metasurfaces. In addition to the reciprocal condition, we will impose the lossless behavior by considering all the element of the impedance matrix to be purely imaginary, i.e., $Z_{ij} = jX_{ij}$. By putting all these constraints into Eq. (A8), the equation can be found to be exactly the same as Eq. (16). The solution to the impedance components are therefore the same as Eqs. (17-19).

APPENDIX B: TRANSFER MATRIX OF A SECTOR OF WEDGE-SHAPED MATERIAL

Here we consider an acoustic notation as an example, for TE-polarized EM waves, the results are equivalent. For waves propagating in isotropic and homogeneous material, the fields generated by a monopole source located at the center can be written as

$$p = XH_0^{(2)}(kr) + YH_0^{(1)}(kr) \tag{B1}$$

$$\begin{aligned} v = -\frac{1}{2\mathrm{j}Z_0}\{&X[H_{-1}^{(2)}(kr) - H_1^{(2)}(kr)] \\ &+ Y[H_{-1}^{(1)}(kr) - H_1^{(1)}(kr)]\}\end{aligned} \tag{B2}$$

The transfer matrix is defined as

$$\begin{bmatrix} p_i \\ S_1 v_i\end{bmatrix} = \begin{bmatrix} M_{11} & M_{12} \\ M_{21} & M_{22}\end{bmatrix}\begin{bmatrix} p_o \\ S_2 v_o\end{bmatrix}. \tag{B3}$$

where the subscripts denote the fields at the input port r_1 and output port r_2. To calculate these values, we first impose that $v_o = 0$, so that $M_{11} = p_i/p_o$ and $M_{21} = S_1 v_i/p_o$. This condition is satisfied when

$$\frac{Y}{X} = \alpha = -\frac{H_{-1}^{(2)}(kr_2) - H_1^{(2)}(kr_2)}{H_{-1}^{(1)}(kr_2) - H_1^{(1)}(kr_2)} \tag{B4}$$

Then M_{11} and M_{21} can be calculated as

$$M_{11} = \frac{H_0^{(2)}(kr_1) + \alpha H_0^{(1)}(kr_1)}{H_0^{(2)}(kr_2) + \alpha H_0^{(1)}(kr_2)} \tag{B5}$$

$$\begin{aligned} M_{21} = -\frac{S_1}{2\mathrm{j}Z_0}[&\frac{H_{-1}^{(2)}(kr_1) - H_1^{(2)}(kr_1)}{H_0^{(2)}(kr_2) + \alpha H_0^{(1)}(kr_2)} \\ &+ \alpha\frac{H_{-1}^{(1)}(kr_1) - H_1^{(1)}(kr_1)}{H_0^{(2)}(kr_2) + \alpha H_0^{(1)}(kr_2)}]\end{aligned} \tag{B6}$$

Similarly, we can impose that $p_o = 0$, so that $M_{12} = p_i/S_2 v_o$ and $M_{22} = S_1 v_i/S_2 v_o$. This condition is satisfied when

$$\frac{Y}{X} = \beta = -\frac{H_0^{(2)}(kr_2)}{H_0^{(1)}(kr_2)} \tag{B7}$$

Then M_{12} and M_{22} can be calculated as

$$M_{12} = -\frac{2\mathrm{j}Z_0}{S_2}\frac{H_0^{(2)}(kr_1) + \beta H_0^{(1)}(kr_1)}{H_{-1}^{(2)}(kr_2) - H_1^{(2)}(kr_2) + \beta[H_{-1}^{(1)}(kr_2) - H_1^{(1)}(kr_2)]} \tag{B8}$$

$$M_{22} = \frac{S_1}{S_2}\frac{H_{-1}^{(2)}(kr_1) - H_1^{(2)}(kr_1) + \beta[H_{-1}^{(1)}(kr_1) - H_1^{(1)}(kr_1)]}{H_{-1}^{(2)}(kr_2) - H_1^{(2)}(kr_2) + \beta[H_{-1}^{(1)}(kr_2) - H_1^{(1)}(kr_2)]} \tag{B9}$$

Hence the transfer matrices can be calculated by assigning the corresponding input and output positions.

The impedance matrix can be calculated with Eq. (40).

For a given finite-thickness metasurface with fixed r_1 and r_2, there are only two variables: k and Z_0 (essentially ρ and κ for acoustics and ϵ and μ for EM waves). However, the derived requirement for the metasurface shows 3 components to control (Z_{11}, Z_{12}, and Z_{22}). Therefore, conventional GSL-based metasurfaces by phase shifting with high index media cannot fulfill the requirements, even with ideally matched characteristic impedance. To realize the required impedance matrix profile, we need another degree of freedom, which is the bianisotropy, or Willis coupling within the unit cells.

APPENDIX C: CONVERSION FROM SCATTERING MATRIX TO TRANSFER MATRIX

The schematics is shown in Fig.D1 . The transfer matrix of an arbitrary structure in a wedge-shaped waveguide is defined in Eq. (B3), and the scattering matrix is defined as

$$\begin{bmatrix} B \\ C \end{bmatrix} = \begin{bmatrix} S_{11} & S_{12} \\ S_{21} & S_{22} \end{bmatrix} \begin{bmatrix} A \\ D \end{bmatrix}. \tag{C1}$$

Calculation strategy of the transfer matrix is the same as in Appendix B, where we first set $v_o = 0$ to obtain M_{11} and M_{21}. In this case we have $\frac{D}{C} = \alpha$ and

$$\frac{A}{C} = \frac{1 - S_{22}\alpha}{S_{21}} \tag{C2}$$

$$\frac{B}{C} = \frac{1 - S_{22}\alpha}{S_{21}} S_{11} + S_{12}\alpha \tag{C3}$$

where α is defined in Eq. (B4). Then M_{11} and M_{21} can be expressed in terms of S matrix:

$$M_{11} = \frac{(1 - S_{22}\alpha)H_0^{(2)}(kr_1) + (S_{11} - S_{11}S_{22}\alpha + S_{21}S12\alpha)H_0^{(1)}(kr_1)}{S_{21}H_0^{(2)}(kr_2) + S_{21}\alpha H_0^{(1)}(kr_2)} \tag{C4}$$

$$M_{21} = -\frac{S_1}{2\mathrm{j}Z_0} \frac{(1 - S_{22}\alpha)[H_{-1}^{(2)}(kr_1) - H_1^{(2)}(kr_1)] + (S_{11} - S_{11}S_{22}\alpha + S_{21}S12\alpha)[H_{-1}^{(1)}(kr_1) - H_1^{(1)}(kr_1)]}{S_{21}H_0^{(2)}(kr_2) + S_{21}\alpha H_0^{(1)}(kr_2)} \tag{C5}$$

Similarly, we can impose that $p_o = 0$, in which case

$$\frac{A}{C} = \frac{1 - S_{22}\beta}{S_{21}} \tag{C6}$$

$$\frac{B}{C} = \frac{1 - S_{22}\beta}{S_{21}} S_{11} + S_{12}\beta \tag{C7}$$

where β is defined in Eq. (B7).so that $M_{12} = p_i/S_2 v_o$ and $M_{22} = S_1 v_i/S_2 v_o$ can be expressed as

$$M_{12} = -\frac{2\mathrm{j}Z_0}{S_2} \frac{(1 - S_{22}\beta)H_0^{(2)}(kr_1) + (S_{11} - S_{11}S_{22}\beta + S_{21}S12\beta)H_0^{(1)}(kr_1)}{S_{21}[H_{-1}^{(2)}(kr_2) - H_1^{(2)}(kr_2)] + S_{21}\beta[H_{-1}^{(1)}(kr_2) - H_1^{(1)}(kr_2)]} \tag{C8}$$

$$M_{22} = \frac{S_1}{S_2} \frac{(1 - S_{22}\beta)[H_{-1}^{(2)}(kr_1) - H_1^{(2)}(kr_1)] + (S_{11} - S_{11}S_{22}\beta + S_{21}S12\beta)[H_{-1}^{(1)}(kr_1) - H_1^{(1)}(kr_1)]}{S_{21}[H_{-1}^{(2)}(kr_2) - H_1^{(2)}(kr_2)] + S_{21}\beta[H_{-1}^{(1)}(kr_2) - H_1^{(1)}(kr_2)]} \tag{C9}$$

APPENDIX D: CALCULATION OF THE MATRICES IN THE SIMULATION

For the ease of implementation, the method we used to retrieve the impedance matrix in COMSOL is inspired by the standard 4-microphone method for acoustic experiments with impedance tubes, whose setups are shown in Fig. D1. The waves in the upstream and downstream can be written as

$$p_{\mathrm{up}} = AH_0^{(2)}(kr) + BH_0^{(1)}(kr) \tag{D1}$$

$$p_{\mathrm{down}} = CH_0^{(2)}(kr) + DH_0^{(1)}(kr) \tag{D2}$$

The positions of 4 microphones are x_1, x_2, x_3, x_4, respectively. By performing two measurements with different boundary conditions at the end of the tube, we can obtain four independent equations for the determination of the four transfer matrix elements. Two different boundaries we used at the end of the tube are plane

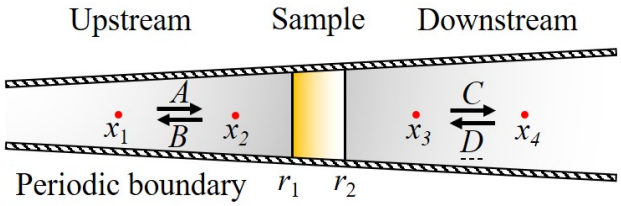

FIG. D1. Setups for the measurement of samples in a wedge shaped waveguide.

wave radiation (condition #1) and hard wall (condition #2). The pressure detected by these microphones under these two boundary conditions are noted as $p_m^{(n)}$ where m denotes the number of the microphone and n denotes the number of the boundary condition. They satisfy the condition:

$$\begin{bmatrix} H_0^{(2)}(kx_1) & H_0^{(1)}(kx_1) \\ H_0^{(2)}(kx_2) & H_0^{(1)}(kx_2) \end{bmatrix} \begin{bmatrix} A^{(1)} & A^{(2)} \\ B^{(1)} & B^{(2)} \end{bmatrix} = \begin{bmatrix} p_1^{(1)} & p_1^{(2)} \\ p_2^{(1)} & p_2^{(2)} \end{bmatrix} \tag{D3}$$

Similarly,

$$\begin{bmatrix} H_0^{(2)}(kx_3) & H_0^{(1)}(kx_3) \\ H_0^{(2)}(kx_4) & H_0^{(1)}(kx_4) \end{bmatrix} \begin{bmatrix} C^{(1)} & C^{(2)} \\ D^{(1)} & D^{(2)} \end{bmatrix} = \begin{bmatrix} p_3^{(1)} & p_3^{(2)} \\ p_4^{(1)} & p_4^{(2)} \end{bmatrix} \tag{D4}$$

With the measurement of $p_m^{(n)}$ under two different conditions, all the ABCD in the matrices can be calculated. Therefore, the scattering matrix can be calculated as

$$S = \begin{bmatrix} B^{(1)} & B^{(2)} \\ C^{(1)} & C^{(2)} \end{bmatrix} \begin{bmatrix} A^{(1)} & A^{(2)} \\ D^{(1)} & D^{(2)} \end{bmatrix}^{-1} \tag{D5}$$

If the inner radius and outer radius of the metasurface is r_1 and r_2, then the pressure and volume velocity at both sides can be written as:

$$\begin{bmatrix} p_i^{(1)} & p_i^{(2)} \\ S_1 v_i^{(1)} & S_1 v_i^{(2)} \end{bmatrix} = \begin{bmatrix} H_0^{(2)}(kr_1) & H_0^{(1)}(kr_1) \\ -\frac{S_1}{2\mathrm{j}Z_0}[H_{-1}^{(2)}(kr_1) - H_1^{(2)}(kr_1)] & -\frac{S_1}{2\mathrm{j}Z_0}[H_{-1}^{(1)}(kr_1) - H_1^{(1)}(kr_1)] \end{bmatrix} \begin{bmatrix} A^{(1)} & A^{(2)} \\ B^{(1)} & B^{(2)} \end{bmatrix} \tag{D6}$$

$$\begin{bmatrix} p_o^{(1)} & p_o^{(2)} \\ S_2 v_o^{(1)} & S_2 v_o^{(2)} \end{bmatrix} = \begin{bmatrix} H_0^{(2)}(kr_2) & H_0^{(1)}(kr_2) \\ -\frac{S_2}{2\mathrm{j}Z_0}[H_{-1}^{(2)}(kr_2) - H_1^{(2)}(kr_2)] & -\frac{S_2}{2\mathrm{j}Z_0}[H_{-1}^{(1)}(kr_2) - H_1^{(1)}(kr_2)] \end{bmatrix} \begin{bmatrix} C^{(1)} & C^{(2)} \\ D^{(1)} & D^{(2)} \end{bmatrix} \tag{D7}$$

The transfer matrix of the measured unit cell can thus be calculated as

$$T = \begin{bmatrix} p_o^{(1)} & p_o^{(2)} \\ S_2 v_o^{(1)} & S_2 v_o^{(2)} \end{bmatrix} \begin{bmatrix} p_i^{(1)} & p_i^{(2)} \\ S_1 v_i^{(1)} & S_1 v_i^{(2)} \end{bmatrix}^{-1} \tag{D8}$$

Hence the impedance matrix can is calculated as

$$Z = \begin{bmatrix} -\frac{T_{22}}{T21} & -\frac{1}{T21} \\ \frac{T_{12}T_{21} - T_{11}T_{22}}{T21} & -\frac{T_{11}}{T21} \end{bmatrix} \tag{D9}$$

[1] N. Enghetaand R. W. Ziolkowski, *Metamaterials: physics and engineering explorations* (John Wiley & Sons, 2006).
[2] S. A. Cummer, J. Christensen, and A. Alù, Controlling sound with acoustic metamaterials, Nature Reviews Materials **1**, 16001 (2016).
[3] H.-T. Chen, A. J. Taylor, and N. Yu, A review of metasurfaces: physics and applications, Reports on Progress in Physics **79**, 076401 (2016).
[4] S. B. Glybovski, S. A. Tretyakov, P. A. Belov, Y. S. Kivshar, and C. R. Simovski, Metasurfaces: From microwaves to visible, Physics Reports **634**, 1 (2016).
[5] A. Pors, M. G. Nielsen, R. L. Eriksen, and S. I. Bozhevolnyi, Broadband focusing flat mirrors based on plasmonic gradient metasurfaces, Nano letters **13**, 829 (2013).
[6] N. Yu, P. Genevet, M. A. Kats, F. Aieta, J.-P. Tetienne, F. Capasso, and Z. Gaburro, Light propagation with phase discontinuities: generalized laws of reflection and refraction, science **334**, 333 (2011).
[7] A. V. Kildishev, A. Boltasseva, and V. M. Shalaev, Planar photonics with metasurfaces, Science **339**, 1232009 (2013).
[8] A. Arbabi, E. Arbabi, Y. Horie, S. M. Kamali, and A. Faraon, Planar metasurface retroreflector, Nature Photonics **11**, 415 (2017).
[9] Y. Yao, R. Shankar, M. A. Kats, Y. Song, J. Kong, M. Loncar, and F. Capasso, Electrically tunable metasurface perfect absorbers for ultrathin mid-infrared optical modulators, Nano letters **14**, 6526 (2014).
[10] X. Ni, Z. J. Wong, M. Mrejen, Y. Wang, and X. Zhang, An ultrathin invisibility skin cloak for visible light, Science **349**, 1310 (2015).
[11] X. Ni, A. V. Kildishev, and V. M. Shalaev, Metasurface holograms for visible light, Nature communications **4**, 2807 (2013).

[12] G. Zheng, H. Mühlenbernd, M. Kenney, G. Li, T. Zentgraf, and S. Zhang, Metasurface holograms reaching 80% efficiency, Nature nanotechnology **10**, 308 (2015).

[13] J. P. Wong, A. Epstein, and G. V. Eleftheriades, Reflectionless wide-angle refracting metasurfaces, IEEE Antennas and Wireless Propagation Letters **15**, 1293 (2016).

[14] V. S. Asadchy, M. Albooyeh, S. N. Tcvetkova, A. Díaz-Rubio, Y. Ra'di, and S. Tretyakov, Perfect control of reflection and refraction using spatially dispersive metasurfaces, Physical Review B **94**, 075142 (2016).

[15] A. Epsteinand G. V. Eleftheriades, Synthesis of passive lossless metasurfaces using auxiliary fields for reflectionless beam splitting and perfect reflection, Physical review letters **117**, 256103 (2016).

[16] N. M. Estakhriand A. Alù, Wave-front transformation with gradient metasurfaces, Physical Review X **6**, 041008 (2016).

[17] A. Díaz-Rubio, V. S. Asadchy, A. Elsakka, and S. A. Tretyakov, From the generalized reflection law to the realization of perfect anomalous reflectors, Science advances **3**, e1602714 (2017).

[18] A. Díaz-Rubioand S. Tretyakov, Acoustic metasurfaces for scattering-free anomalous reflection and refraction, Physical Review B **96**, 125409 (2017).

[19] J. Li, C. Shen, A. Díaz-Rubio, S. A. Tretyakov, and S. A. Cummer, Systematic design and experimental demonstration of bianisotropic metasurfaces for scattering-free manipulation of acoustic wavefronts, Nature Communications **9**, 1342 (2018).

[20] M. B. Muhlestein, C. F. Sieck, P. S. Wilson, and M. R. Haberman, Experimental evidence of willis coupling in a one-dimensional effective material element, Nature communications **8**, 15625 (2017).

[21] V. S. Asadchy, A. Díaz-Rubio, and S. A. Tretyakov, Bianisotropic metasurfaces: physics and applications, Nanophotonics **7**, 1069 (2018).

[22] Y. Liu, Z. Liang, F. Liu, O. Diba, A. Lamb, and J. Li, Source illusion devices for flexural lamb waves using elastic metasurfaces, Physical review letters **119**, 034301 (2017).

[23] D. Baresch, J.-L. Thomas, and R. Marchiano, Observation of a single-beam gradient force acoustical trap for elastic particles: acoustical tweezers, Physical review letters **116**, 024301 (2016).

[24] H. He, M. Friese, N. Heckenberg, and H. Rubinsztein-Dunlop, Direct observation of transfer of angular momentum to absorptive particles from a laser beam with a phase singularity, Physical Review Letters **75**, 826 (1995).

[25] J. Wang, J.-Y. Yang, I. M. Fazal, N. Ahmed, Y. Yan, H. Huang, Y. Ren, Y. Yue, S. Dolinar, M. Tur, *et al.*, Terabit free-space data transmission employing orbital angular momentum multiplexing, Nature photonics **6**, 488 (2012).

[26] C. Shi, M. Dubois, Y. Wang, and X. Zhang, High-speed acoustic communication by multiplexing orbital angular momentum, Proceedings of the National Academy of Sciences **114**, 7250 (2017).

[27] N. Jiménez, R. Picó, V. Sánchez-Morcillo, V. Romero-García, L. M. García-Raffi, and K. Staliunas, Formation of high-order acoustic bessel beams by spiral diffraction gratings, Physical Review E **94**, 053004 (2016).

[28] C. J. Naify, C. A. Rohde, T. P. Martin, M. Nicholas, M. D. Guild, and G. J. Orris, Generation of topologically diverse acoustic vortex beams using a compact metamaterial aperture, Applied Physics Letters **108**, 223503 (2016).

[29] X. Jiang, Y. Li, B. Liang, J.-c. Cheng, and L. Zhang, Convert acoustic resonances to orbital angular momentum, Physical review letters **117**, 034301 (2016).

[30] L. Marrucci, C. Manzo, and D. Paparo, Optical spin-to-orbital angular momentum conversion in inhomogeneous anisotropic media, Physical review letters **96**, 163905 (2006).

[31] A. M. Yaoand M. J. Padgett, Orbital angular momentum: origins, behavior and applications, Advances in Optics and Photonics **3**, 161 (2011).

[32] P. Schemmel, G. Pisano, and B. Maffei, Modular spiral phase plate design for orbital angular momentum generation at millimetre wavelengths, Optics express **22**, 14712 (2014).

[33] S. Tretyakov, *Analytical modeling in applied electromagnetics* (Artech House, 2003).

[34] Y. Li, S. Qi, and M. B. Assouar, Theory of metascreen-based acoustic passive phased array, New Journal of Physics **18**, 043024 (2016).